A novel FeCrMoCSi metallic glass with excellent corrosion resistance and *in vitro* cellular response for biomedical applications

Informative title:

Novel biomedical Fe metallic glass

Kaiyang Li[a], Luxin Liang[a], Qianli Huang[a], Jian Xiao[b,*], Yingtao Tian[c], Hong Wu[a,**]

[a] State Key Laboratory of Powder Metallurgy, Central South University, Changsha 410083, China

[b] Department of Pharmacy, Xiangya Hospital, Central South University, Changsha, 410008, China

[c] Engineering Department, Lancaster University, Lancaster, LA1 4YW, UK

* Corresponding author. admanoas@163.com (Jian Xiao)

** Corresponding author. hwucsu@csu.edu.cn, wuhong927@126.com (Hong Wu)

Abstract

The corrosion resistance and biocompatibility of a novel $Fe_{50}Cr_{18}Mo_{10}C_{20}Si_2$ metallic glass (Fe-MG) are studied by electrochemical measurements and indirect contacting cytotoxicity assays for biomedical applications. In Hank's solution, the Fe-MG shows better corrosion resistance than SS316L, evidenced by the larger polarization resistance in the potentiodynamic and electrochemical impedance spectroscopy (EIS) tests, and the lower amounts of released metallic ions during the immersion test. X-ray photoelectron spectroscopy (XPS) analyses show that a double-layer passive film consisting of outer Fe-rich oxide and inner Cr-rich oxide is formed on the Fe-MG. The stable passive film, together with the defect-free nature of the metallic glass, accounts for good corrosion resistance. In addition, *in vitro* tests suggest that the Fe-MG extracts have good blood compatibility and no cytotoxicity to murine fibroblast cells. Compared with other Fe-based metallic glasses, the prepared novel Fe-MG contains no toxic elements and shows a low corrosion rate.

Keywords: metallic glass; microstructure; corrosion; biocompatibility; blood compatibility.

1. Introduction

In the biomedical field, stainless steel (SS for short) has been widely used for bone fixing screws, plates, intravascular stents and other biomedical components due to its good mechanical property, low cost, moderate corrosion resistance and good biocompatibility. For long-term usage, however, SS may suffer from severe corrosions or even implant failure due to the general and/or localized degradations in the aggressive body environments. Post-implantation inspection showed that up to 90% SS316L (a typical biomedical SS) exhibited general corrosion and localized failure like pitting, crevice corrosion and stress corrosion cracking [1]. The corrosion of SS is always accompanied by the release of metallic ions (like Fe^{2+}/Fe^{3+}, Ni^{2+} and Cr^{6+}), which may introduce allergenic reactions and toxicity to the human body [2, 3]. For instance, previous *in vitro* and animal studies have proved that Ni^{2+} and Cr^{6+} could be a potential carcinogen [3, 4]. These observations motivated the pursuit of implant materials with better biocompatibility and higher corrosion resistance.

Due to its amorphous nature, metallic glass (MG) is free from grain boundaries, segregations and crystal defects like dislocation, which enable it to have excellent mechanical and anti-corrosion properties [5-8]. Besides, metallic glass has good net-shaping behavior. These benefits make metallic glass a promising candidate to replace existing metallic biomaterials. In the last decade, a series of metallic glasses, including Zr-based [9, 10], Ti-based [11], Pt-based [5] and Fe-based [12], have been developed for biomedical applications. They are fabricated into rods, plates, wires, stents, or thin films for bio-functional purposes, including load-bearing, anti-wear, improved cellular response, antibacterial, and so on [5, 13]. For instance, copper mold cast Ti-Zr-Cu-Pd-Sn bulk metallic glass (BMG) had a critical diameter as high as 10 mm and exhibits good plasticity, high yield strength and fracture strength [14]. Zr-Cu-Ag thin film metallic glass (TFMG) was fabricated by different methods (physical vapor deposition or magnetron sputtering) and the effect of element contents on microstructure and biocide activity was investigated [15-18].

Among different metallic glasses, Fe-based metallic glasses stand out for biocompatible applications owing to their high strength and hardness, excellent corrosion and wear resistance, and the relatively low-priced Fe as the main element. It is reported that Fe-based metallic glasses have a high hardness up to 1800 MPa and ultimate tensile strength of ~3000 MPa, which are much higher than currently used biomedical steels [13]. To overcome the brittle nature of Fe-based metallic glasses, the ductility could be improved by carefully adjusting the chemical composition [19]. For instance, the plastic strain of Cu-Zr-Ti metallic glass increased greatly with the addition of 2.2 at.% Fe-C [20]. Zhou et al. [21] found that the plastic strain of Fe-Mo-P-C-B BMG was improved from 1.7% to 7% with the proper addition of 1 at.% Si. However, further increasing Si to 2 at.% resulted in brittle fracture without any plastic deformation [21]. Besides, Fe-based metallic glasses show much higher corrosion resistance than stainless steels in the corrosive body fluids, as reported in several studies [22]. Wang et al. [23] fabricated a nickel-free $Fe_{41}Co_7Cr_{15}Mo_{14}C_{15}B_6Y_2$ metallic glass by suction copper mold casting, which had a good glass-forming ability (GFA) and exhibited much better corrosion performance than SS316L in Hank's solution and artificial saliva. Zohdi et al. [24] investigated the corrosion performance of a $Fe_{55-x}Cr_{18}Mo_7B_{16}C_4Nb_x$ system and found that the addition of Nb not only improved the GFA of this system, but also enhanced its corrosion resistance in Ringer's solution. For biomedical implant applications, the Fe-Cr-Mo series metallic glasses are proposed as promising candidates [13] due to their high GFA and good corrosion resistance. During the interaction with body fluids, such Cr-containing Fe-Cr-Mo metallic glasses spontaneously develop a passive film mainly composed of chromium oxide/hydroxide on the surface [22], and the presence of Mo helps to improve corrosion resistance [25]. On the basis of Fe-Cr-Mo, improvement has been made in this metallic glass system by adding alloying elements to acquire certain improved properties [13]. To improve the GFA, previous studies chose elements Y, Co or B, which are known to be toxic and may potentially be hazardous to human health in the long term [26]. Therefore, novel Fe-based metallic glasses are still highly desired

and being developed by many researchers. A successful metallic glass design should consider several aspects. First, the added element should increase, or at least maintain, the GFA. Second, the selected element should be of low toxicity to avoid any adverse reaction with human body. Third, the properties (corrosion, mechanical, and/or anti-bacterial) of the metallic glass could be improved rather than deteriorated. Based on these criteria and the element mixing rule in previous studies, C and Si are considered as alloying elements due to their non-toxic nature, the beneficial role in improving GFA and corrosion resistance [27]. By far, the Fe-Cr-Mo-C-Si metallic glass has not been reported. Then, it is of great interest to successfully prepare such metallic glass with specific chemical compositions and examine the related properties. In addition, an in-depth understanding of the corrosion mechanism and detailed analyses of the passive oxide film during corrosion are highly desired, since it could be helpful in the optimized design of implant metallic glass with better corrosion resistance.

In the present study, a Fe-based metallic glass (Fe-Cr-Mo-C-Si) free from toxic elements is fabricated. The corrosion resistance is evaluated in simulated body fluids by electrochemical techniques and immersion tests. Detailed microstructure of the passive film and chemical state of each element are analyzed by XPS. Besides, standardized *in vitro* cytotoxicity tests are also conducted to evaluate the biocompatibility for its potential biomedical usage.

2. Experimental

2.1 Material preparation

Ingots of $Fe_{50}Cr_{18}Mo_{10}C_{20}Si_{2}$ alloy were prepared by melting high purity (>99.9 wt.%) elements in an arc-melting furnace with a non-consumable tungsten electrode and water-cooled copper hearth. The furnace was firstly flushed with pure argon thoroughly and pure Ti ingot was used as a getter prior to melting to reduce the residual oxygen as much as possible. At least five remelting steps were carried out and the ingot was

slipped into the hearth after each remelting to ensure microstructural homogeneity. Then, $Fe_{50}Cr_{18}Mo_{10}C_{20}Si_2$ metallic glass (Fe-MG for short) rod samples with a diameter of 1.5 mm were fabricated by water-cooled copper mold suction casting. The rods were vertically cut along the diameter to show the cross-section for further studies. Biomedical SS316L samples were purchased from Kanghui Medical Innovation Co. Ltd. (Changzhou, China). All the sample surfaces were mechanically polished up to 2000 grit by wet SiC paper, washed with distilled water, cleaned in an ultrasonic bath with acetone, and dried with pressurized air.

2.2 Corrosion tests

Corrosion resistance was measured by both electrochemical and immersion tests. Hank's Balanced Salt Solution (Hank's solution for short), with a measured pH value of 7.4 and the concentrations of 8.0 NaCl, 0.4 KCl, 0.18 $CaCl_2$, 0.35 $NaHCO_3$, 0.1 $MgSO_4 \cdot 7H_2O$, 0.1 $MgCl_2 \cdot 6H_2O$, 0.12 Na_2HPO_4, 0.06 KH_2PO_4 and 1.0 glucose (all in g L^{-1}), was used to simulate the body fluid. The electrochemical corrosion tests were conducted in a conventional three-electrode chemical cell on an electrochemical station (PARSTAT 400, Princeton). The counter, reference and working electrodes are platinum plate, saturated calomel electrode (SCE) and SS316L/Fe-MG sample, respectively. The testing temperature was kept at 37 ± 0.5 °C using a water bath, and Hank's solution was aerated. Open circuit potential (OCP) measurement was maintained to 7200 s for a steady state with the variation on potential less than 0.01 V/h [28]. Then, electrochemical impedance spectroscopy (EIS) was applied in the frequency range between 10^{-2} Hz and 10^5 Hz with an amplitude of ± 10 mV to the open-circuit potential. After EIS, the polarization curves were recorded from -1.0 to 1.6 V (vs. SCE) with a scan rate of 1 mV s^{-1}. The corrosion potential (E_{corr}), corrosion current density (I_{corr}) and pitting potential (E_{pit}) were estimated from the polarization curves. All the electrochemical measurements were carried out in triplicate and the results were expressed as "mean values $\pm$ standard deviation". The corrosion rate could be estimated by the electrochemical parameters based on ASTM G102-89 [29]:

$$\text{Corr. rate} = 3.27 \cdot \frac{i_{corr}}{\rho} \cdot EW \qquad\qquad \text{Equation 1}$$

where Corr.rate is the corrosion rate in μm y^{-1}; EW is the alloy equivalent weight; i_{corr} is the corrosion current density, mA cm^{-3}; ρ is the density of the alloy, g cm^{-3}.

The immersion test was performed in Hank's solution at 37 °C under the guidance of ASTM G31 [30]. The SS316L and Fe-MG specimens were immersed separately in Hank's solution with a solution/surface area ratio of 20 mL/cm^2. After 30 days' static immersion, the samples were taken out and the concentrations of dissolved ions in Hank's solution were measured by an inductively coupled plasma atomic emission spectrometry (ICP-AES, Leeman). All the measurements were repeated three times.

2.3 Materials characterization

X-ray Diffraction (XRD, Dmax 2500VB with Cu-Kα radiation) was carried out with a scan rate of 4° min^{-1} at room temperature to detect the phase constitution of the prepared Fe-MG. Differential Scanning Calorimetry (DSC, NETZSCH STA 449C) was used to identify the thermodynamic properties of the prepared Fe-MG at a scan rate of 20 K min^{-1} in Ar atmosphere. A Scanning Electron Microscope (SEM, FEI Quanta FEG250) equipped with Energy Dispersive Spectrometer (EDS) was used to identify the chemical composition of the as-prepared Fe-MG and observe the surface morphologies of SS316L and Fe-MG after the electrochemical tests. X-ray photoelectron spectroscopy (XPS, ESCALAB 250Xi) was employed to conduct surface analyses of the Fe-MG after the immersion in Hank's solution for 30 days. The XPS characterization was conducted with mono Al Kα (1486.6 eV) radiation at a vacuum pressure of 10^{-9} bar, 15 kV and 15 mA. The binding energy was calibrated using C 1s hydro-carbon peak at 284.4 eV. The depth profile of the corroded Fe-MG surface was obtained by in-situ XPS ion beam sputtering with Ar$^+$. The Ar$^+$ etch rate was estimated to be 0.08 nm s^{-1} based on comparative measurements on SiO$_2$.

2.4 Cytotoxicity evaluation

Murine fibroblast cells (NIH-3T3) were cultured in Dulbecco's modified Eagle's medium (DMEM) supplemented with 10% fetal bovine serum (FBS), 100 U mL^{-1} penicillin, and 100 μg mL^{-1} streptomycin at 37 °C in a humidified atmosphere with 5% CO_2. The cytotoxicity test was performed by indirect contact. Extraction medium was prepared using DMEM serum-free medium with a surface area/extraction medium ratio of 1.25 cm^2 mL^{-1} in a humidified atmosphere with 5% CO_2 at 37 °C for 72 h. After the extracts were centrifuged, the supernatant was withdrawn and restored at 4 °C as the culture medium. DMEM medium was used as a negative control and DMEM medium + 10% Dimethylsulfoxide (DMSO) was set as a positive control. Cells were incubated in 96-well cell culture plates at the density of approximately 5×10^3 cells per 100 μL culture medium for 24 h and then replaced by 100 μL of extraction medium. After 1, 2 and 4 days' incubation, the 96-well plates were observed under an optical microscope. 10 μL of MTT (3-(4,5-dimethylthiazol-2-yl)-2,5-diphenyltetrazolium bromide) was added to each well and the cells were cultured for 4 h in the incubator. Thereafter, 100 μL of formazan solubilization solution (10% sodium dodecyl sulfate in 0.01 M HCl) was added to each well and restored in the incubator for more than 10 h. The spectro-photometrical absorbance of the specimens was measured with a microplate reader (Bio-RAD680) at 570 nm.

2.5 Hemolysis test

The hemolysis test was conducted under a strict protocol at Xiangya Hospital with the beforehand ethics approval and guidance of the ethics committee. Healthy human blood extracted from a volunteer (with 3.8 wt.% citric acid sodium as anticoagulant) was diluted by physiological saline with a volume ratio of 4:5. SS316L and Fe-MG were separately immersed in centrifugal tubes with 10 mL physiological saline at 37 °C for 30 min. Then, 0.2 ml of diluted blood was added to each centrifugal tube and the mixtures were kept at 37 °C for 60 min. In the same way, a negative control group with physiological saline solution and a positive group with deionized water were prepared. Then, all the tubes were centrifuged at 3000 rpm for 5 min. Supernatant was transferred

to a 96-well cell culture plates and the absorbance (AB) was determined by a microplate reader at a wavelength of 545 nm. Hemolysis of samples was calculated by the following equation [31]:

$$Hemolysis = \frac{AB_{test} - AB_{negative\ control}}{AB_{positive\ control} - AB_{negative\ control}} \times 100\% \qquad Equation\ 2$$

3. Results

3.1 Amorphous structure

Figure 1(a) shows the XRD patterns of Fe-MG. The typical amorphous features can be confirmed by the absence of Bragg peaks representing crystalline structure, together with the broad scattering signals from 40° to 50°. As shown in Figure 1(b), the prepared Fe-MG has a smooth surface with no obvious crystal defects. EDS analyses were randomly taken on ten places of the sample and a typical result is shown in Figure 1(c). It can be seen that the actual composition of the prepared Fe-MG is very close to its nominal composition. These results indicate that the as-prepared $Fe_{50}Cr_{18}Mo_{10}C_{20}Si_2$ metallic glass is homogeneous in nature and composed of a single glassy phase.

The glass structure of the Fe-MG was further confirmed by the DSC curves and shown in Figure 1(d). At a heating rate of 20 K min^{-1}, the as-prepared sample shows a clear glass transition, followed by an extended supercooled liquid region and two exothermic peaks for a two-stage crystallization process. The glass transition temperature (T_g), onset crystallization temperature (T_x) and supercooled liquid value ΔT_x ($\Delta T_x = T_x - T_g$) obtained from the DSC curve were 870, 916 and 46 K, respectively. The wide supercooled liquid region, i.e., the ΔT_x value of 46 K, indicates the high GFA and resistance to crystallization of the as-prepared Fe-MG [26].

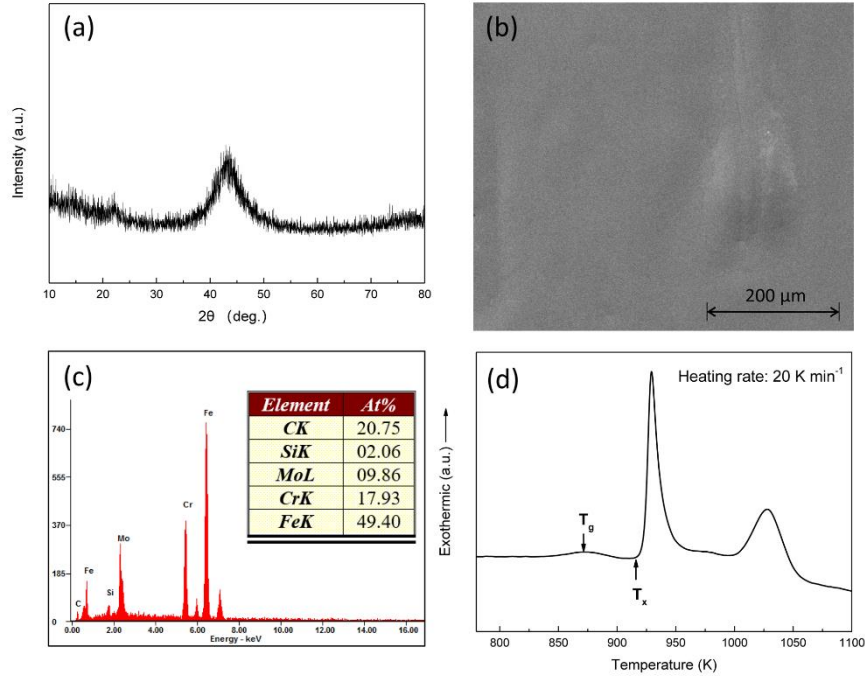| Element	At%
CK	20.75
SiK	02.06
MoL	09.86
CrK	17.93
FeK	49.40

Figure 1. (a) XRD pattern, (b) SEM surface morphology, (c) a typical EDS analysis of the chemical composition, and (d) DSC curves of the Fe-MG.

3.2 Corrosion behavior

Figure 2(a) shows the OCP as a function of immersion time obtained by exposing SS316L and Fe-MG samples in Hank's solution. The potentials of both samples slightly increased during the initial period (0-1000 s), indicating the growth of the passive oxide film. The potentials then become rather steady until the end of the measurement, which was resulted from a quite stable surface condition on both samples. The steady OCP of Fe-MG is over 0.1 V while the corresponding value of SS316L is -0.17 V. The higher OCP of Fe-MG indicates a more stable and noble surface oxide layer.
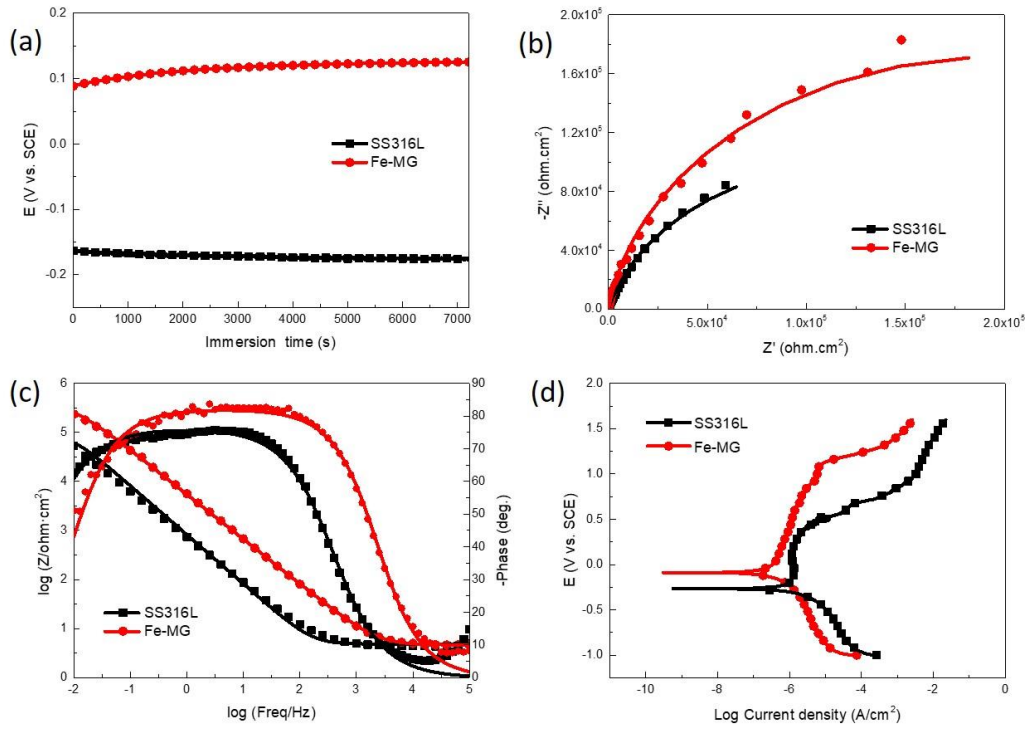
Figure 2. Representative (a) OCP curves, EIS spectra (b) Nyquist diagram and (c) Bode diagram, (d) potentiodynamic polarization curves of SS316L and Fe-MG in Hank's solution at 37 °C.

The impedance spectra for SS316L and Fe-MG samples after 7200 s' immersion in Hank's solution are shown in Figure 2(b) and (c) as Nyquist and Bode diagrams, respectively. Based on the Nyquist plot (Figure 2(b)), Fe-MG has a semicircle diameter larger than that of SS316L, indicating a greater corrosion resistance [32]. In Bode diagram (Figure 2(c)), both specimens have similar patterns, i.e., the impedance shows a slope of about -1 as a capacitive behavior of the passive film in the low- and middle-frequency range. Besides, Fe-MG has an absolute impedance value higher than SS316L in the whole frequency range. For the phase angle, both specimens approach 0° at high frequency as solution resistance; then remains around -80° in the middle-frequency range as a typical passive film on the surface and its near capacitive response; in the low frequency, the phase angle drops to a lower value due to the contribution of the passive film resistance [33].

Based on the above analyses, the $R_s(QR_p)$ model with one-time constant was applied to describe the oxide film formed on the alloy surfaces during immersion in the simulated body fluid. In this model, the element Q is a constant phase element (CPE) and fined as $Q_{CPE}=(C(j\omega)n)]^{-1}$, where C is the capacitance of an ideal capacitor if n =1; j is the current; ω is the frequency; n is the exponent of constant phase element and $0<n<1$ represents the deviation from an ideal capacitor [34]. R_s and R_p represent the resistance of the test electrolyte and the passive film, respectively [35]. The low chi-square (χ^2) values prove that the simulated data is in good agreement with the experimental one. Table 1 shows the parameters obtained from the fitting results. It is found that Fe-MG presents higher R_p and lower Q values than those of SS316L in Hank's solution, indicating that Fe-MG has higher impedance values and a more corrosion-resistant oxide film than those of SS316L.

Table 1. Electrochemical impedance parameters obtained by $R_s(QR_P)$ model of the equivalent circuits for SS316L and Fe-MG.

	R_s (Ω cm^2)	R_p (10^5 Ω cm^2)	Q (Ω^{-1} s^n cm^{-2})	n	χ^2
SS316L	3.15 ± 0.02	1.26 ± 0.15	$2.463 \pm 0.017 \times 10^{-4}$	0.922 ± 0.002	0.0077
Fe-MG	4.62 ± 0.08	3.94 ± 0.09	$3.452 \pm 0.021 \times 10^{-5}$	0.912 ± 0.001	0.0025

Figure 2(d) presents the potentiodynamic polarization curves of SS316L and Fe-MG in Hank's solution at 37 °C. The corrosion potential (E_{corr}), pitting potential (E_{pit}) and corrosion current density (I_{corr}) are estimated from these curves and shown in Table 2. Both SS316L and Fe-MG exhibit a low corrosion current density (I_{corr}) in the order of 10^{-7} A cm^{-2}. The passivation region E_{pass} is defined as $E_{pass}=E_{pit}-E_{corr}$ and the polarization curves of both specimens exhibit a stable passivation region. Yet Fe-MG has a much higher E_{pit} and wider passivation region E_{pass} than SS316L, indicating the

higher stability of the passive film formed on Fe-MG. Figure 3 shows the representative SEM surface morphologies of SS316L and Fe-MG after potentiodynamic polarization in Hank's solution. Several pits appeared on the surface of SS316L with diameters of 100-200 μm. For Fe-MG, only small pits with diameters of several μm were observed, indicating the higher resistance to pitting.

Table 2. The results of potentiodynamic parameters of SS316L and Fe-MG in Hank's solution.

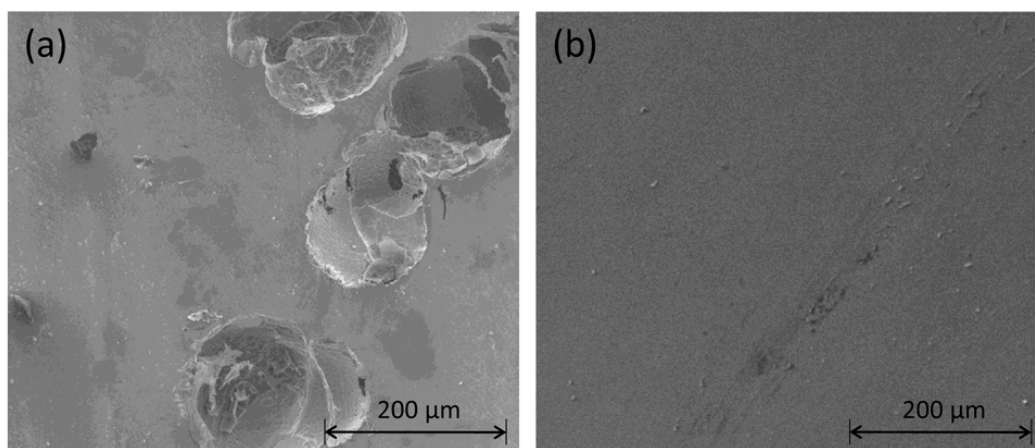|	I_{corr} (10^{-7} A cm^{-2})	E_{corr} (V vs. SCE)	E_{pit} (V vs. SCE)	E_{pass}
SS316L	4.63 ± 0.82	-0.253 ± 0.020	0.293 ± 0.014	0.546
Fe-MG	2.39 ± 0.32	-0.045 ± 0.011	1.072 ± 0.017	1.027

Figure 3. SEM micrographs of (a) SS316L and (b) Fe-MG after potentiodynamic polarization tests in Hank's solution.

Metallic ion released into the body fluid is also an important aspect during the biocompatibility evaluation of metallic implants. To further investigate the corrosion behaviors of the specimens, static immersion tests of SS316L and Fe-MG were carried out in Hank's solution at 37 °C and the released metallic ion was measured by ICP-MS after 30 days (shown in Table 3). For SS316L, Fe, Cr and Ni ions were detected at the level below 0.1 μg mL^{-1}. For Fe-MG, only Fe ion was detected as a low concentration

of 0.01 μg mL^{-1}, possibly due to the fact that the concentration of other ions fell below the detection limit. The more stable oxide passive film formed on Fe-MG may contribute to the higher corrosion resistance and the inhibition of ion release, which suggests its great potential in biomedical applications.

Table 3. The concentrations (μg mL^{-1}) of ions released from SS316L and Fe-MG after static immersion in Hank's solution for 30 days.

Alloy	Fe	Cr	Ni	Mo
SS316L	0.06	0.01	0.02	--
Fe-MG	0.01	--	--	--

--: not detected.

To elucidate the microstructural characteristics and element distribution of the passive film formed on Fe-MG, XPS analyses were performed on the specimen after 30 days' immersion in Hank's solution. The spectra of Fe 2p, Cr 2p, Mo 3d, Si 2p and O 1s for the samples without Ar-ion sputtering are depicted in Figure 4. The survey spectra in Figure 4 contains all the compositional elements and oxygen. As shown in Figure 4(b), the Fe 2p spectrum is composed of two sets of doublet peaks corresponding to $2p_{1/2}$ and $2p_{3/2}$ peaks of metallic and oxide states. The detection of Fe^0 peak (707.5 ± 0.1 eV) suggests the incorporation of metallic state Fe from the substrate and the thickness of the passive film is at nano scale. The oxide states of iron are FeO (708.4 ± 0.1 eV) and Fe$_2$O$_3$ (711. ± 0.3 eV). The peaks of Cr $2p_{1/2}$ and Cr $2p_{3/2}$ in Figure 4(c) represent metallic Cr (573.8 ± 0.1 eV), Cr$_2$O$_3$ (576.2 ± 0.1 eV) and Cr(OH)$_3$ (577.2 ± 0.2 eV). For Mo 3d peaks, the spin-obit coupling of Mo $3d_{5/2}$ and Mo $3d_{3/2}$ leads to doublet, and the details are shown in Figure 4(d), i.e., metallic state Mo^0 (227.6 ± 0.1 eV for $3d_{5/2}$ and 227.6 ± 0.1 eV for $3d_{3/2}$), Mo^{4+} (229.3 ± 0.1 eV for $3d_{5/2}$ and 232.4 ± 0.1 eV for $3d_{3/2}$) and Mo^{6+} (232.5 ± 0.1 eV for $3d_{5/2}$ and 235.6 ± 0.1 eV for $3d_{3/2}$) [36]. The peak intensity of metallic state Mo is relatively larger than that of the oxide states, indicating the enrichment of metallic Mo under the passive film [37, 38]. Si 2p at 99.08 eV and

101.48 eV proves that Si is not only in its elemental status Si^0, but also in oxidized status as SiO_x. The O 1s peak at different binding energy positions indicates O is in its metal oxides, OH^- and H_2O states.
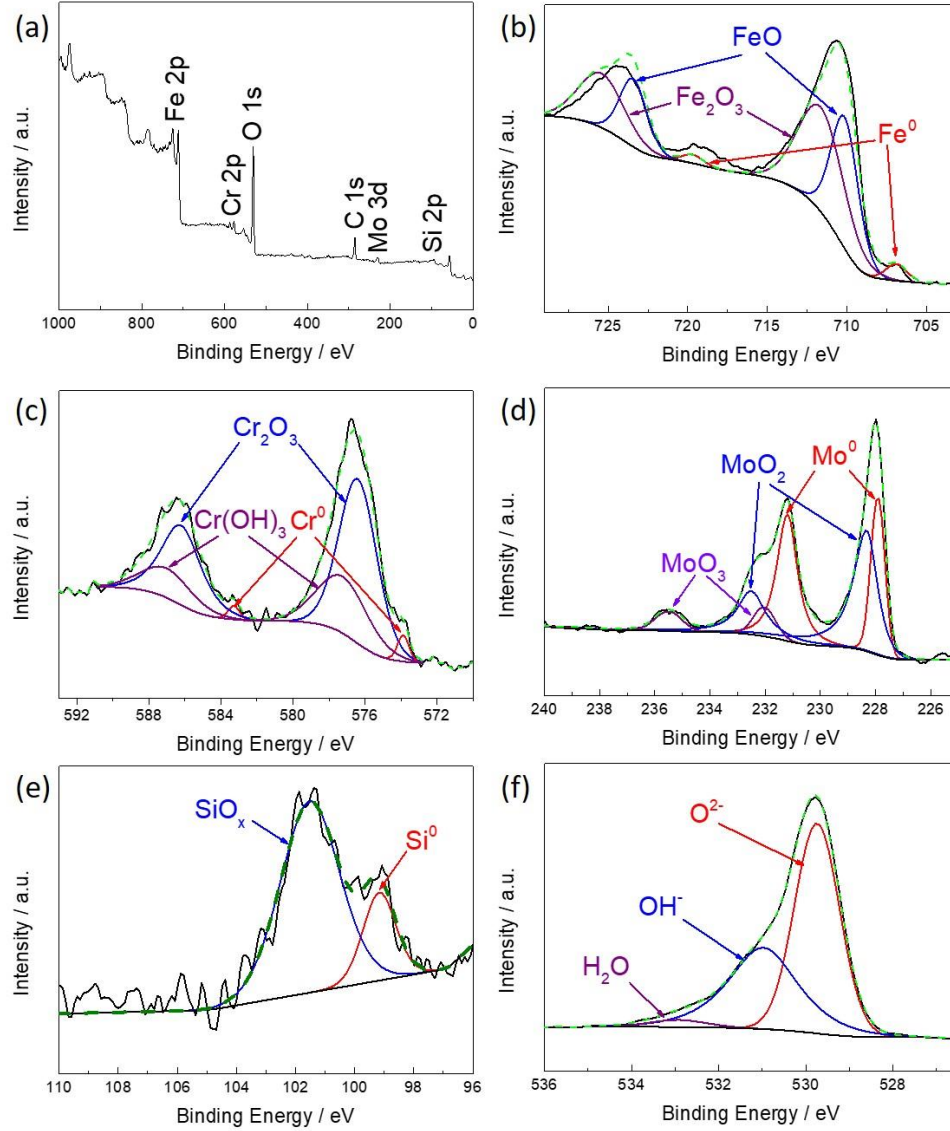

Figure 4. XPS analyses of Fe-MG sample surface after 30 days' immersion in Hank's solution: (a) whole survey spectra, (b) Fe 2p, (c) Cr 2p, (d) Mo 3d, (e) Si 2p, and (f) O 1s.

The concentration depth profiles of component elements in the passive films and underlying substrate of the Fe-MG are shown in Figure 5. The C performs a similar compositional variation trend except for its accumulation at the 0 nm position, which

might be caused by carbon-containing contaminates. Clearly, during the immersion period, the Fe-MG formed a bi-layer structure, including an outer Fe-rich oxide layer and an inner Cr/Mo-rich oxide layer. Comparing with the nominal compositions of the alloys, Si is slightly enriched in the passive films. The total thickness of the passive oxide film was about 10 nm.
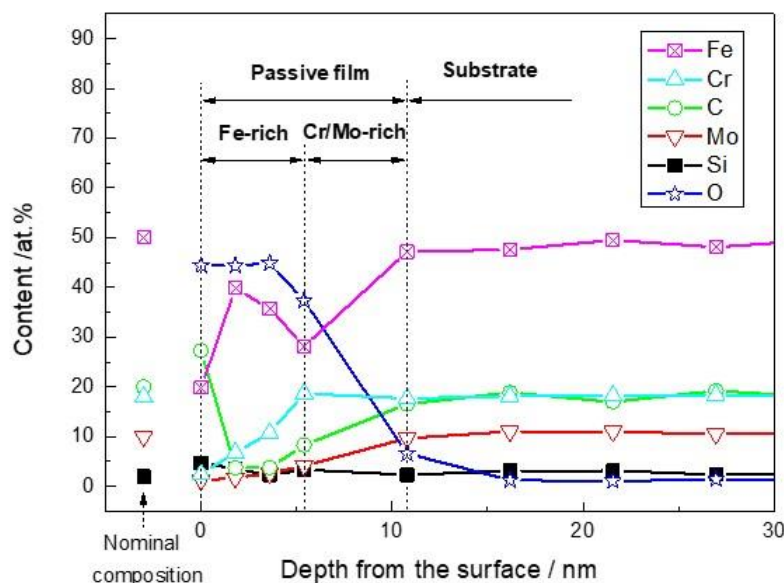

Figure 5. Depth profiles of element concentration in the passive films formed on Fe-MG after 30 days' immersion in Hank's solution.

3.3 Indirect cytotoxicity evaluation

An ideal candidate material for implantation should have minimum unintended interference to the surrounding tissues. Figure 6(a) shows the results of MTT assay using NIH 3T3 cells grown in SS316L and Fe-MG extracts for 1, 2 and 4 days. These data are expressed as cell viability and are related to the negative control, which is considered to correspond to 100% viable cells. It can be observed that both SS316L and Fe-MG extracts exhibit good cell growth for the testing periods (1, 2 and 4 days) after cell implantation with high viability of almost 100%. No significant difference in cell viability was observed in analyzed materials in comparison with the negative control. Based on ISO 10993-5:2009, the Fe-MG exhibits cytotoxicity of Grade 0-1 [39]. Figure

6(b) shows the NIH3T3 cell morphologies at each checking time. It can be seen that cell number grows quickly during the 4-day culture period for all groups, and there is no obvious difference between the negative and experimental groups. Most cells appear elongated in a spindle shape and become longitudinally aligned at high cell densities. As shown in Figure 6(c), the hemolysis ratios of SS316L and Fe-MG are all below 1%, indicating excellent blood compatibility [40].
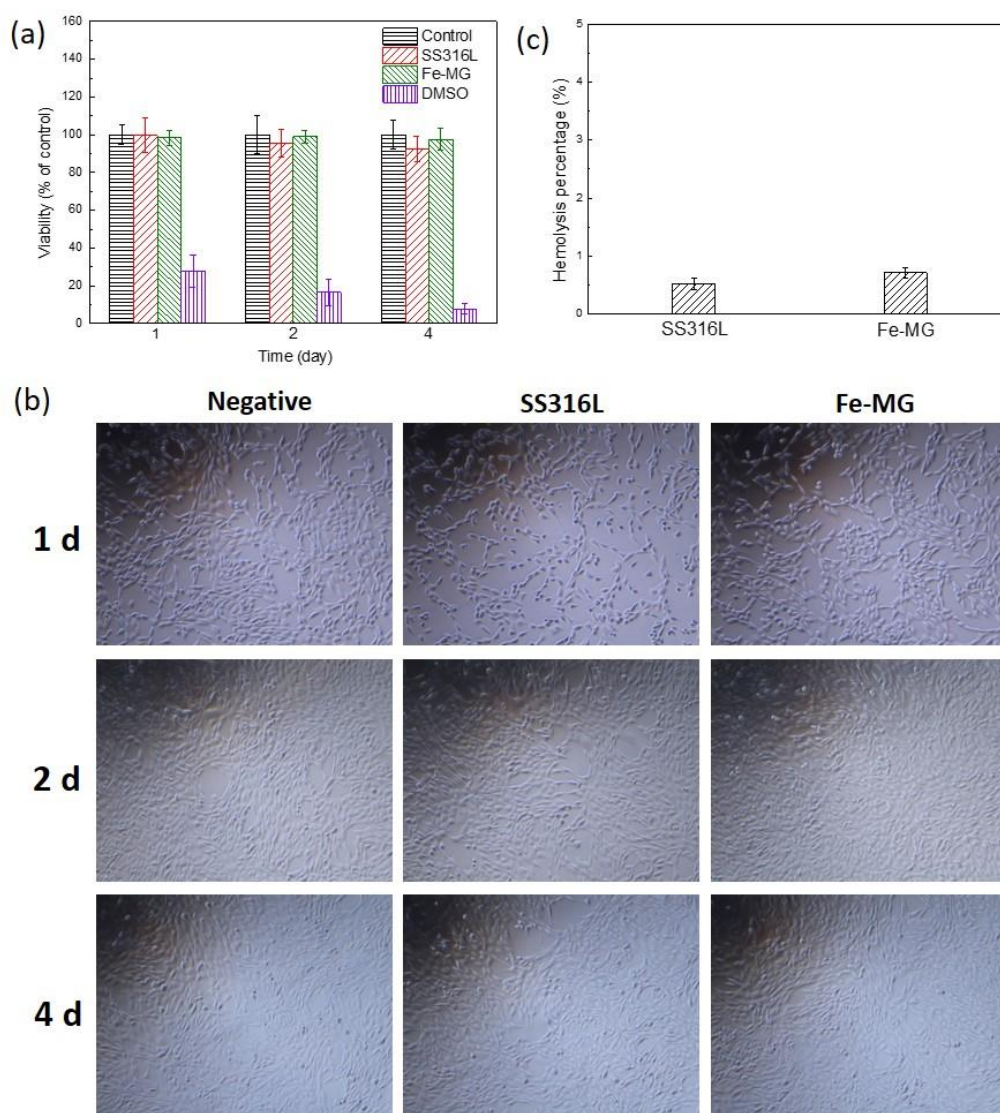

Figure 6. (a) MTT results for indirect cytotoxicity tests for SS316L and Fe-MG extracts using NIH3T3 cells, (b) NIH-3T3 cell morphologies after 1, 2 and 4 days' culture in SS316L and Fe-MG extraction medium, (c) Hemolysis percentage of SS316L and Fe-MG.

4. Discussion

A good biomaterial for long-term implant service in human body should exhibit a combination of good feasibility, processability, excellent corrosion resistance and biocompatibility [41-43]. The following section will try to summarize the promising application of Fe-MG as implant materials from fabrication, corrosion resistance and cytotoxicity points of view.

4.1 Glass-forming ability (GFA)

The successful application of metallic glass greatly lies in its GFA, which is often reflected by several empirical aspects, including multi-elements, large mismatch of atomic size, and negative mixing heat among different elements [44]. The present Fe-MG system meets the multi-element criteria with three types of alloying elements, which are late transition metal (Fe), early transition metals (Cr, Mo) and metalloids (C, Si). The atomic size of the constituent elements varies significantly and decreases in the order of Mo > Cr > Fe > Si > C [45]. Besides, the mixing heats of atomic pairs Fe-Cr/Mo, Fe-Si/C, Cr/Mo-Si/C all have negative values within the range of -1 ~ -45 kJ mol^{-1} [46]. It is generally believed that these features can help suppress the nucleation and growth of a crystalline phase and stabilize the supercooled liquid during the formation process of amorphous structure. Thus, the Fe-Cr-Mo-C-Si metallic glass with low nucleation probability, nearly non-crystal-growth reactions and low atomic diffusivity could have a low liquidus temperature, leading to the high ΔT_x value of 46 K and high GFA. These features provide the Fe-MG with a good processability. Therefore, it can be easily fabricated to complex shapes by direct casting, and/or further accurately processed by thermoplastic forming due to its wide temperature region as glass state [47]. Thus, the Fe-MG should be suitable to be made for most of the biomedical devices used both *in vivo* and *in vitro*.

4.2 Corrosion resistance and biocompatibility

High corrosion resistance of bio-inert metallic materials is the key factor in ensuring implant safety, which demands a very stable surface to survive the complex body fluid environment [48]. SS316L has a long clinical history as bio-inert metallic material. However, due to the aggressive attacks by Cl⁻ in the biological environments and the presence of crystal defects (such as MnS inclusion, dislocation, grain boundary) [49], SS316L frequently suffers from corrosion issues like pitting and the consequent release of toxic ions (e.g., Ni^{2+}) with extended time [50, 51]. Based on the potentiodynamic polarization curve in Figure 2(b), a rapid increase in the current density occurred at a relatively low potential value (0.546 V as E_{pit}) for SS316L, indicating its comparatively higher tendency of pitting corrosion. On the contrary, the breakdown potential of Fe-MG is about 1.027 V, indicating its high pitting resistance. Further, the lower corrosion current density of Fe-MG proves its higher resistance to general corrosion than SS316L. All these results showed that the Fe-MG possesses a stable passive fil, and high pitting resistance, which would make them much safer than SS316 L when used in human body.

The improved resistance to both general and localized corrosion of the Fe-MG in this study could be attributed to the amorphous nature and the formation of a stable oxide passive film during the interaction with simulated body fluid. The metallic glass has a homogenous amorphous microstructure and even distributions of elements. It also does not contain crystal defects such as grain boundaries or precipitates, which might be pitting initiation sites upon the exposure to fluids containing Cl⁻. Besides, metallic glass has a single phase, which holds alloying elements in an equilibrium state beyond the solubility limits. Such over-saturated structure could facilitate the selective oxidation of easily passivating elements like Cr and Mo. Cr is the typical passivating element in alloys and the corresponding chromium oxides/hydroxides have high stability and can remain intact even after long-period immersion in human body fluid. Mo could further improve corrosion resistance by incorporating the chromium oxides/hydroxides and thereafter increase its stability [38, 52]. Alternatively, Mo may dissolve in the nearby solution and then redeposit on the surface oxide to cover the active sites and prevents

further corrosion [53]. Based on the XPS characterization in Figure 5, the corrosion-inhibiting effect of Mo seems to be achieved by participating in the passive film growth rather than the dissolution-redeposition mechanism, since no obvious accumulation of Mo is found on the top oxide layer. While both SS316L and Fe-MG contain Cr and Mo, the higher Mo content in Fe-MG as 10 at.% ensures the higher stability of the formed passive film. What is more, the presence of metalloid elements (C and Si) is beneficial to the kinetics of passivation and the optimization of passive film composition [54]. C could accelerate the active dissolution before forming the passive film, thus resulting in the accumulation of protective elements (Cr and Mo) in the passive film and the improved corrosion resistance [22]. The XPS depth profile detects a slight enrichment of oxidized Si in the passive film, which is known to act as a barrier and keep the metallic components from dissolution.

The stable oxide film formed on Fe-MG is also beneficial to good biocompatibility, which is mainly determined by the chemical state of the passive film and the concentration of released ions during the interaction with body fluids. In general, if a large number of ions are released within a short period of time due to severe corrosion of the metallic implants, it could potentially change the redox state of the cells and disturb the protein from normal functioning [55-58], i.e., leading to cellular toxicity. The formation of a stable surface oxide film could reduce ion release and maintain the biological safety of implant materials. The Fe-MG shows better corrosion resistance and a more stable passive oxide film. Therefore, it can be a more promising candidate material for implants. Besides, the Fe-MG does not contain toxic elements like Ni, B, Be, and Y, which will be safer than conventional materials.

Due to the good corrosion resistance, several Fe-Cr-Mo metallic glasses, including Fe-Cr-Mo-Co-C-B-Y [23], Fe-Cr-Mo-P-C [26] and Fe-Cr-Mo-B-C-Nb [59], have been developed as promising biomedical materials to replace SS316L. Table 4 presents a detailed summary of these Fe-based metallic glasses and the corrosion rates are

calculated based on Equation 1. Comparing with previously developed systems, the Fe-MG in the current study has a high corrosion potential, low corrosion current and corrosion rate, indicating its high corrosion resistance. Besides, the absence of rare earth elements (Y, Er) or other possible toxic elements like B further reduces its potential hazard to implanted host from a long-term point of view. Further long-term *in vitro* and *in vivo* tests could be carried out to confirm its excellent biocompatibility and controllable release of ions.

Table 4. Comparison of *in vitro* corrosion properties of biomedical Fe-based metallic glass in Hank's or Ringer's solution.

Composition (at.%)	Solution	E_{corr} (mV)	I_{corr} ($\times 10^{-7}$ A cm^{-2})	Corr. rate (μm y^{-1})	Ref.
$Fe_{55}Cr_{18}Mo_7B_{16}C_4$		-169	24.66	28.7	
$Fe_{52}Cr_{18}Mo_7B_{16}C_4Nb_3$	Ringer's	-45	1.995	2.3	[24]
$Fe_{51}Cr_{18}Mo_7B_{16}C_4Nb_4$		122	0.380	0.4	
$Fe_{60}Cr_{10}Mo_{10}P_{13}C_7$		-317±13	4.92±0.18	5.7	
$Fe_{55}Cr_{20}Mo_5P_{13}C_7$	Hank's	-306±15	2.65±0.13	3.1	[26]
$Fe_{50}Cr_{20}Mo_{10}P_{13}C_7$		-309±17	3.79±0.10	4.4	
$Fe_{41}Co_7Cr_{15}Mo_{14}C_{15}B_6Y_2$	Hank's	-269±12	2.376±0.532	2.8	[23]
$Fe_{32}Ni_{36}Cr_{14}P_{12}B_6$	Hank's	-176	184	17.5	[60]
$Fe_{67}Co_{18}B_{14}Si_1$		-697	620	59.2	
$Fe_{41}Co_7Cr_{15}Mo_{14}C_{15}B_6Y_2$		-270±10	2.34±0.53	2.7	
$(Fe_{44}Cr_5Co_5Mo_{13}Mn_{11}C_{16}B_6)_{98}Y_2$	Hank's	-230±30	2.880±1.19	3.3	[61]
$Fe_{48}Cr_{15}Mo_{14}C_{15}B_6Er_2$		-300±70	0.90±0.17	1.0	
$Fe_{77}Mo_5P_9C_{7.5}B_{1.5}$ composite	Hank's	-910	46.8	49	[62]
$Fe_{50}Cr_{18}Mo_{10}C_{20}Si_2$	Hank's	-45±11	2.39±0.32	3.9	Current study

5. Conclusions

In the current study, a novel Fe-based metallic glass $Fe_{50}Cr_{18}Mo_{10}C_{20}Si_2$ has been prepared with a homogeneous amorphous structure and high GFA. With higher pitting potential, lower corrosion current density and higher impedance in the simulated body fluid, $Fe_{50}Cr_{18}Mo_{10}C_{20}Si_2$ metallic glass exhibit higher corrosion resistance than SS316L. The passive film is composed of Fe-rich outer layer and Cr-Mo-rich oxide

inner layer. Besides, the good cellular response and blood compatibility of $Fe_{50}Cr_{18}Mo_{10}C_{20}Si_2$ metallic glass could be attributed to the protective effect of the passive film, which can successfully prevent the metal ions from releasing into the simulated body fluid. Compared with other Fe-based metallic glass, the $Fe_{50}Cr_{18}Mo_{10}C_{20}Si_2$ has no toxic elements and high corrosion resistance, indicating its promising application in the biomedical field.

Acknowledgement

Conflicts of interest or competing interests

The authors declare that they have no known competing financial interests or personal relationships that could have appeared to influence the work reported in this paper.

Data and code availability

The raw/processed data required to reproduce these findings cannot be shared at this time due to technical or time limitations. Concurrently, the data also forms part of an ongoing study.

Reference

[1]   N   K.,   Corrosion   of   metallic   implants.   (1987)   Br.   Corros.   J.   22:   272. Doi:10.1179/000705987798271352

[2]   L Reclaru, H Lüthy, R Ziegenhagen, P-Y Eschler, A Blatter, Anisotropy of nickel release and corrosion in austenitic stainless steels. (2008) Acta Biomater. 4: 680. Doi:10.1016/j.actbio.2007.10.008

[3]   H Wu, L Liang, X Lan, et al., Tribological and biological behaviors of laser cladded Ti-based metallic glass composite coatings. (2020) Appl. Surf. Sci. 507. Doi:10.1016/j.apsusc.2019.145104

[4]   A Doran, F Law, M Allen, N Rushton, Neoplastic transformation of cells by soluble but not particulate forms of metals used in orthopaedic implants. (1998) Biomaterials 19: 751. Doi:10.1016/S0142-9612(97)00209-3

[5]   J Schroers, G Kumar, TM Hodges, S Chan, TR Kyriakides, Bulk metallic glasses for biomedical applications. (2009) JOM 61: 21. Doi:10.1007/s11837-009-0128-1

[6]   H Wu, L Liang, H Zeng, et al., Microstructure and nanomechanical properties of Zr-based bulk metallic glass composites fabricated by laser rapid prototyping. (2019) Mater. Sci. Eng., A 765: 1. Doi:10.1016/j.msea.2019.138306

[7]   H Wu, I Baker, Y Liu, X Wu, PR Munroe, J Zhang, Tribological studies of a Zr-based bulk metallic glass. (2013) Intermetallics 35: 25. Doi:10.1016/j.intermet.2012.11.010

[8]   H Wu, I Baker, Y Liu, X Wu, PR Munroe, Effects of environment on the sliding tribological behaviors of Zr-based bulk metallic glass. (2012) Intermetallics 25: 115. Doi:10.1016/j.intermet.2011.12.025

[9]   L Liu, C Qiu, M Sun, Q Chen, K Chan, GK Pang, Improvements in the plasticity and biocompatibility of Zr–Cu–Ni–Al bulk metallic glass by the microalloying of Nb. (2007) Mater. Sci. Eng., A 449: 193. Doi:10.1016/j.msea.2006.02.255

[10] H Wu, I Baker, Y Liu, X-l Wu, Dry sliding tribological behavior of Zr-based bulk metallic glass. (2012) Trans. Nonferrous Met. Soc. China 22: 585. Doi:10.1016/s1003-6326(11)61217-x

[11] Y Wang, H Li, Y Cheng, Y Zheng, L Ruan, In vitro and in vivo studies on Ti-based bulk metallic glass as potential dental implant material. (2013) Mater. Sci. Eng., C 33: 3489. Doi:10.1016/j.msec.2013.04.038

[12] H Wu, X-d Lan, Y Liu, et al., Fabrication, tribological and corrosion behaviors of detonation gun sprayed Fe-based metallic glass coating. (2016) Trans. Nonferrous Met. Soc. China 26: 1629. Doi:10.1016/s1003-6326(16)64271-1

[13] H Li, Y Zheng, Recent advances in bulk metallic glasses for biomedical applications. (2016) Acta Biomater. 36: 1. Doi:10.1016/j.actbio.2016.03.047

[14] SL Zhu, XM Wang, A Inoue, Glass-forming ability and mechanical properties of Ti-based bulk glassy alloys with large diameters of up to 1cm. (2008) Intermetallics 16: 1031. Doi:10.1016/j.intermet.2008.05.006

[15] A Etiemble, C Der Loughian, M Apreutesei, et al., Innovative Zr-Cu-Ag thin film metallic glass deposed by magnetron PVD sputtering for antibacterial applications. (2017) J. Alloys Compd. 707: 155. Doi:10.1016/j.jallcom.2016.12.259

[16] GI Nkou Bouala, A Etiemble, C Der Loughian, C Langlois, JF Pierson, P Steyer, Silver influence on the antibacterial activity of multi-functional Zr-Cu based thin film metallic glasses. (2018) Surf. Coat. Technol. 343: 108. Doi:10.1016/j.surfcoat.2017.10.057

[17] S Comby-Dassonneville, T Venot, A Borroto, et al., ZrCuAg Thin-Film Metallic Glasses: Toward Biostatic Durable Advanced Surfaces. (2021) ACS Appl. Mater. Interfaces 13: 17062. Doi:10.1021/acsami.1c01127

[18] B Subramanian, S Maruthamuthu, ST Rajan, Biocompatibility evaluation of sputtered zirconium-based thin film metallic glass-coated steels. (2015) Int J Nanomedicine 10 Suppl 1: 17. Doi:10.2147/IJN.S79977

[19] XJ Gu, SJ Poon, GJ Shiflet, M Widom, Ductility improvement of amorphous steels: Roles of shear modulus and electronic structure. (2008) Acta Mater. 56: 88. Doi:10.1016/j.actamat.2007.09.011

[20] AH Cai, Y Feng, DW Ding, et al., Effect of Fe-C alloy additions on properties of Cu-Zr-Ti metallic glasses. (2019) J. Alloys Compd. 798: 273. Doi:10.1016/j.jallcom.2019.05.256

[21] J Zhou, B Sun, Q Wang, Q Yang, W Yang, B Shen, Effects of Ni and Si additions on mechanical properties and serrated flow behavior in FeMoPCB bulk metallic glasses. (2019) J. Alloys Compd. 783: 555. Doi:10.1016/j.jallcom.2018.12.331

[22] CAC Souza, DV Ribeiro, CS Kiminami, Corrosion resistance of Fe-Cr-based amorphous alloys: An overview. (2016) J. Non-Cryst. Solids 442: 56. Doi:10.1016/j.jnoncrysol.2016.04.009

[23] Y Wang, H Li, Y Cheng, S Wei, Y Zheng, Corrosion performances of a Nickel-free Fe-based bulk metallic glass in simulated body fluids. (2009) Electrochem. Commun. 11: 2187. Doi:10.1016/j.elecom.2009.09.027

[24] H Zohdi, H Shahverdi, S Hadavi, Effect of Nb addition on corrosion behavior of Fe-based metallic glasses in Ringer's solution for biomedical applications. (2011) Electrochem. Commun. 13: 840. Doi:10.1016/j.elecom.2011.05.017

[25] MW Tan, E Akiyama, H Habazaki, A Kawashima, K Asami, K Hashimoto, The role of chromium and molybdenum in passivation of amorphous Fe-Cr-Mo-P-C alloys in deaerated 1 M HCl. (1996) Corros. Sci. 38: 2137. Doi:10.1016/S0010-938X(96)00071-6

[26] S Li, Q Wei, Q Li, B Jiang, Y Chen, Y Sun, Development of Fe-based bulk metallic glasses as potential biomaterials. (2015) Mater. Sci. Eng., C 52: 235. Doi:10.1016/j.msec.2015.03.041

[27] H Li, Z Lu, S Wang, Y Wu, Z Lu, Fe-based bulk metallic glasses: Glass formation, fabrication, properties and applications. (2019) Prog. Mater. Sci. 103: 235. Doi:10.1016/j.pmatsci.2019.01.003

[28] J Fornell, N Van Steenberge, A Varea, et al., Enhanced mechanical properties and in vitro corrosion behavior of amorphous and devitrified Ti40Zr10Cu38Pd12 metallic glass. (2011) J. Mech. Behav. Biomed. Mater. 4: 1709. Doi:10.1016/j.jmbbm.2011.05.028

[29] ASTM, G102-89 Standard Practice for Calculation of Corrosion Rates and Related Information from Electrochemical Measurements, (2015) ASTM International, West Conshohocken, PA

[30] ASTM, G31-72: Standard Practice for Laboratory Immersion Corrosion Testing of Metals, (2004) ASTM International, West Conshohocken, PA

[31] ASTM, F756-17 Standard practice for assessment of hemolytic properties of materials, (2017) ASTM International, West Conshohocken, PA

[32] S Kannan, A Balamurugan, S Rajeswari, Electrochemical characterization of hydroxyapatite coatings on HNO_3 passivated 316L SS for implant applications. (2005) Electrochim. Acta 50: 2065. Doi:10.1016/j.electacta.2004.09.015

[33] H-Q Fan, D-D Shi, M-M Ding, M-C Li, YF Cheng, Q Li, Preparation of (3-mercaptopropyl)trimethoxylsilane film on brass and its corrosion resistance in natural seawater. (2020) Prog. Org. Coat. 138: 105392. Doi:10.1016/j.porgcoat.2019.105392

[34] Q-Y Wang, Y-R Tang, R Pei, Y-C Xi, S Wan, A study on preparation and corrosion behavior of nano rare earth oxide-modified chromized coatings. (2020) Mater. Corros. 71: 249. Doi:10.1002/maco.201911017

[35] Q-Y Wang, R Pei, S Liu, et al., Microstructure and corrosion behavior of different clad zones in multi-track Ni-based laser-clad coating. (2020) Surf. Coat. Technol. 402: 126310. Doi:10.1016/j.surfcoat.2020.126310

[36] E Gardin, S Zanna, A Seyeux, A Allion-Maurer, P Marcus, XPS and ToF-SIMS characterization of the surface oxides on lean duplex stainless steel – Global and local approaches. (2019) Corros. Sci. 155: 121. Doi:10.1016/j.corsci.2019.04.039

[37] K Asami, K Hashimoto, S Shimodaira, XPS determination of compositions of alloy surfaces and surface oxides on mechanically polished iron-chromium alloys. (1977) Corros. Sci. 17: 713. Doi:10.1016/0010-938X(77)90067-1

[38] K Asami, M Naka, K Hashimoto, T Masumoto, Effect of Molybdenum on the Anodic Behavior of Amorphous Fe-Cr-Mo-B Alloys in Hydrochloric Acid. (1980) J. Electrochem. Soc. 127: 2130.

[39] ISO, 10993–5: 2009 Biological evaluation of medical devices—part 5: tests for in vitro cytotoxicity, (2009),

[40] ASTM, F756-08 Standard practice for assessment of hemolytic properties of materials, (2008) ASTM International, West Conshohocken, PA

[41] T Long, X Zhang, Q Huang, et al., Novel Mg-based alloys by selective laser melting for biomedical applications: microstructure evolution, microhardness and in vitro degradation behaviour. (2017) Virtual Phys. Prototyping 13: 71. Doi:10.1080/17452759.2017.1411662

[42] X Li, L Liang, Y Tan, et al., Using hierarchical mesoporous Mg–Al LDH as a potential model to precisely load BSA for biological application. (2020) J. Micromech. Mol. Phys.: 2050012. Doi:10.1142/S2424913020500125

[43] C Yan, G Ma, A Chen, et al., Additive manufacturing of hydroxyapatite and its composite materials: A review. (2020) J. Micromech. Mol. Phys. 5: 2030002. Doi:10.1142/S2424913020300029

[44] F Zhang, C Zhang, D Lv, J Zhu, W Cao, S Chen, R Schmid-Fetzer, Prediction of Glass Forming Ability Through High Throughput Calculation. (2018) J. Phase Equilib. Diffus. 39: 562. Doi:10.1007/s11669-018-0643-2

[45] JC Slater, Atomic radii in crystals. (1964) J. Chem. Phys. 41: 3199. Doi:10.1063/1.1725697

[46] A Takeuchi, A Inoue, Classification of bulk metallic glasses by atomic size difference, heat of mixing and period of constituent elements and its application to characterization of the main alloying element. (2005) Mater. Trans. 46: 2817. Doi:10.2320/matertrans.46.2817

[47] J Schroers, Processing of bulk metallic glass. (2010) Adv. Mater. 22: 1566. Doi:10.1002/adma.200902776

[48] S Assis, S Rogero, R Antunes, A Padilha, I Costa, A comparative study of the in vitro corrosion behavior and cytotoxicity of a superferritic stainless steel, a Ti－13Nb－13Zr alloy, and an austenitic stainless steel in Hank's solution. (2005) J. Biomed. Mater. Res., Part B 73: 109. Doi:10.1002/jbm.b.30205

[49] N Eliaz, Corrosion of metallic biomaterials: A review. (2019) Mater. 12: 407. Doi:10.3390/ma12030407

[50] M Costa, M Fernandes, Proliferation/differentiation of osteoblastic human alveolar bone cell cultures in the presence of stainless steel corrosion products. (2000) J. Mater. Sci.: Mater. Med. 11: 141. Doi:10.1023/A:1008975507654

[51] S Refaey, F Taha, A El-Malak, Corrosion and inhibition of stainless steel pitting corrosion in alkaline medium and the effect of Cl^- and Br^- anions. (2005) Appl. Surf. Sci. 242: 114. Doi:10.1016/j.apsusc.2004.08.003

[52] P Marcus, On some fundamental factors in the effect of alloying elements on passivation of alloys. (1994) Corros. Sci. 36: 2155. Doi:10.1016/0010-938X(94)90013-2

[53] K Sugimoto, Y Sawada, The role of molybdenum additions to austenitic stainless steels in the inhibition of pitting in acid chloride solutions. (1977) Corros. Sci. 17: 425. Doi:10.1016/0010-938X(77)90032-4

[54] S Pang, T Zhang, K Asami, A Inoue, Bulk glassy Fe–Cr–Mo–C–B alloys with high corrosion resistance. (2002) Corros. Sci. 44: 1847. Doi:10.1016/S0010-938X(02)00002-1

[55] L Liang, Q Huang, H Wu, et al., Stimulation of in vitro and in vivo osteogenesis by Ti-Mg alloys with the sustained-release function of magnesium ions. (2021) Colloids Surf., B 197: 111360. Doi:10.1016/j.colsurfb.2020.111360

[56] S Yang, L Liang, L Liu, et al., Using MgO nanoparticles as a potential platform to precisely load and steadily release Ag ions for enhanced osteogenesis and bacterial killing. (2021) Mater. Sci. Eng., C 119. Doi:10.1016/j.msec.2020.111399

[57] Y Yin, Q Huang, L Liang, et al., In vitro degradation behavior and cytocompatibility of ZK30/bioactive glass composites fabricated by selective laser melting for biomedical applications. (2019) J. Alloys Compd. 785: 38. Doi:10.1016/j.jallcom.2019.01.165

[58] X Lai, E Roberts, Cytotoxicity Effects and Ionic Diffusion of Single-Wall Carbon Nanotubes in Cell Membrane. (2019) J. Micromech. Mol. Phys. Doi:10.1142/S2424913019500061

[59] H Zohdi, M Bozorg, R Arabi Jeshvaghani, H Shahverdi, S Hadavi, Corrosion performance and metal ion release of amorphous and nanocrystalline Fe-based alloys under simulated body fluid conditions. (2013) Mater. Lett. 94: 193. Doi:10.1016/j.matlet.2012.12.051

[60] A Pratap, S Kasyap, S Prajapati, D Upadhyay, Bio-corrosion studies of Fe-based metallic glasses. (2021) Mater. Today: Proc. 42: 1669. Doi:10.1016/j.matpr.2020.07.588

[61] Y Wang, H Li, Y Zheng, M Li, Corrosion performances in simulated body fluids and cytotoxicity evaluation of Fe-based bulk metallic glasses. (2012) Mater. Sci. Eng., C 32: 599. Doi:10.1016/j.msec.2011.12.018

[62] R Liu, R He, J Xiao, M Tang, H Zhang, S Guo, Development of Fe-based bulk metallic glass composite as biodegradable metal. (2019) Mater. Lett. 247: 185. Doi:10.1016/j.matlet.2019.03.118